

# Influence of the approach boundary layer on the flow over an axisymmetric hill at a moderate Reynolds number

M. García-Villalba<sup>a</sup>, J. G. Wissink<sup>b</sup> and W. Rodi<sup>a</sup>

<sup>a</sup>*Karlsruhe Institute of Technology, Germany*

<sup>b</sup>*Brunel University, United Kingdom*

## Abstract

Large Eddy Simulations of a flow at a moderate Reynolds number over and around a three-dimensional hill have been performed. The main aim of the simulations was to study the effects of various inflow conditions (boundary layer thickness and laminar versus turbulent boundary layers) on the flow behind the hill. The main features of the flow behind the hill are similar in all simulations, however various differences are observed. The topology of the streamlines (friction lines) on the surface adjacent to the lower wall was found to be independent of the inflow conditions prescribed and comprised four saddle points and four nodes (of which two are foci). In all simulations a variety of vortical structures could be observed, ranging from a horseshoe vortex - that was formed at the foot of the hill - to a train of large hairpin vortices in the wake of the hill. In the simulation with a thick incoming laminar boundary layer also secondary vortical structures (i.e. hairpin vortices) were observed to be formed at either side of the hill, superposed on the legs of the horseshoe vortex. Sufficiently far downstream of the hill, at the symmetry plane the mean velocity and the rms of the velocity fluctuations were found to become quasi-independent of the inflow conditions, while towards the sides the influence of the hill decreases and the velocity profiles recover the values prevailing at the inflow.

## 1 Introduction

Flow over obstacles occurs in many engineering applications. From a fundamental point of view, the flow over obstacles features a variety of phenomena and is particularly complex: it is three-dimensional (also in the mean), highly unsteady, involves separation and reattachment (possibly at several locations) and contains several interacting vortex systems. Typical examples are flow over axisymmetric obstacles Hunt and Snyder [1980], wall-mounted prismatic obstacles Martinuzzi and Tropea [1993] or finite-height circular cylinders Palau-Salvador et al. [2010]. In the case of obstacles without sharp edges, the separation location is not fixed by the geometry and is highly dependent on the incoming flow characteristics, like Reynolds number or boundary layer thickness. Therefore, it is very challenging to compute accurately this kind of flow.

Recently, a series of experiments performed by Simpson and co-workers Simpson et al. [2002], Byun et al. [2004], Ma and Simpson [2005], Byun and Simpson [2006] renewed the interest in analysing and predicting three-dimensional separation. The configuration they considered was an axisymmetric three-dimensional hill subjected to a turbulent boundary layer. The Reynolds number of the flow based on the free-stream velocity and the height of the hill was relatively high ( $Re = 130000$ ). Since then a number of researchers have tried to reproduce the experimental results using various computational techniques: RANS Wang et al. [2004], Persson et al. [2006], hybrid RANS-LES Tessicini et al. [2007] and pure LES Persson et al. [2006], Patel and Menon [2007], Krajnović [2008], García-Villalba et al. [2009]. It was shown that the RANS predictions were generally poor, while both the hybrid techniques and the pure LES provided promising results although not completely satisfactory. In the simulations reported in García-Villalba et al. [2009], it was observed that, in spite of the high resolution employed, the presence of a thin recirculation region made the flow very sensitive to the grid resolution.

Apart from the grid resolution, one of the most important differences between all computational studies was the modelling of the incoming flow. In the experiment the hill was subjected to a turbulent boundary layer whose thickness was half of the hill height. Because the incoming boundary layer was turbulent, the specification of the inlet conditions had to be done in an unsteady manner. For instance, in García-Villalba et al. [2009] a precursor simulation was used, while in Patel and Menon [2007] a boundary layer profile plus random noise was employed. Because of the high Reynolds number of the flow, it is computationally very expensive to perform parametric studies and, hence, it is very difficult to assess the impact on the results of the modelling of the incoming flow.

In the present paper, we report simulations of flow over the same hill as considered in the previous studies, but at a significantly lower Reynolds number. The aim is to study the influence of the flow characteristics of various approach flows: two simulations with incoming laminar boundary layers of different thicknesses and one simulation with an incoming turbulent boundary layer.

## 2 Numerical model

The LES were performed with the in-house code LESOCC2 (Large Eddy Simulation On Curvilinear Coordinates). The code has been developed at the Institute for Hydromechanics. It is the successor of the code LESOCC developed by Breuer and Rodi [1996] and is described in Hinterberger [2004]. The code solves the Navier-Stokes equations on body-fitted, curvilinear grids using a cell-centered Finite Volume method with collocated storage for the cartesian velocity components and the pressure. Second order central differences are employed for the convection as well as for the diffusive terms. The time integration is performed with a predictor-corrector scheme, where the explicit predictor step for the momentum equations is a low-storage 3-step Runge-Kutta method. The corrector step covers the implicit solution of the Poisson equation for the pressure correction (SIMPLE). The scheme is of second order accuracy in time because the Poisson equation for the pressure correction is not solved during the sub-steps of the Runge-Kutta algorithm in order to save CPU-time. The Rhie and Chow momentum interpolation Rhie and Chow [1983] is applied to avoid pressure-velocity decoupling. The Poisson equation for the pressure-increment is solved iteratively by means of the 'strongly implicit procedure' Stone [1968]. Parallelization is implemented via domain decomposition, and explicit message passing is used with two halo cells along the inter-domain boundaries for intermediate storage.

The configuration mentioned above consists of the flow over and around an axisymmetric hill of height  $H$  and base-to-height ratio of 4. The hill shape is described by:

$$\frac{y(r)}{H} = -\frac{1}{6.04844} \left[ J_0(\Lambda) I_0 \left( \Lambda \frac{r}{2H} \right) - I_0(\Lambda) J_0 \left( \Lambda \frac{r}{2H} \right) \right], \quad (1)$$

where  $\Lambda = 3.1926$ ,  $J_0$  is the Bessel function of the first kind and  $I_0$  is the modified Bessel function of the first kind Simpson et al. [2002]. The approach-flow boundary-layer has a thickness  $\delta$  which varies depending on the simulation (see Table 1). The Reynolds number of the flow based on the free-stream velocity  $U_{ref}$  and the hill height  $H$  is  $Re = 6650$ .

The size of the domain is  $22H \times 6H \times 12H$  in streamwise, wall-normal and spanwise directions, respectively. The grid consists of  $504 \times 256 \times 400$  cells in these directions. The choice of the computational mesh is based on the experience gained in performing an LES of a similar flow problem at a significantly higher  $Re$  García-Villalba et al. [2009], with results compared to experimental data. In order to minimize numerical errors, the grid is quasi-orthogonal close to the hill's surface and the grid points are concentrated in the boundary layer.

As in García-Villalba et al. [2009], the dynamic Smagorinsky subgrid-scale model, first proposed by Germano et al. [1991], has been used in the simulations. The model parameter is determined using an explicit box filter of width equal to twice the mesh size and smoothed by temporal under-relaxation Breuer and Rodi [1996]. The impact of the subgrid-scale model on the

Case	Inflow	$\delta/H$	$Re_\theta$	$C_D$	Line color
S1	Laminar	1	900	0.305	Blue
S2	Laminar	0.1	90	0.493	Green
S3	Turbulent	1	670	0.407	Red

Table 1: Parameters of the simulations.

results is likely to be small. For instance, the maximum values of the ratio of the time-averaged eddy viscosity and the molecular (kinematic) viscosity is  $\langle \nu_{sgs} \rangle / \nu \sim 1$  in the region of interest. For comparison, in García-Villalba et al. [2009] this ratio was  $\langle \nu_{sgs} \rangle / \nu \sim 6$ .

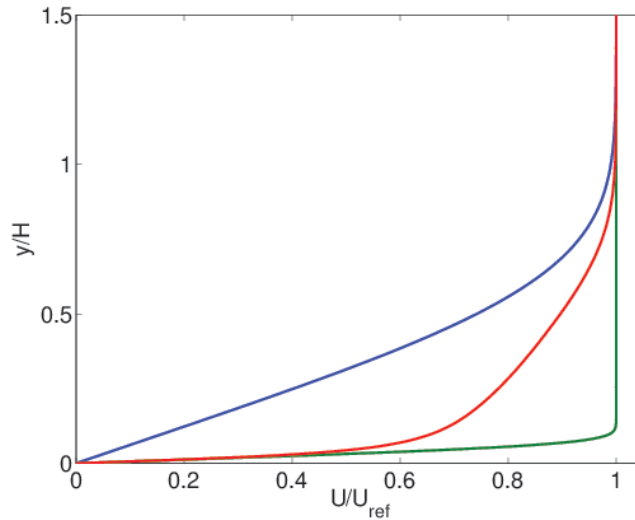


Figure 1: Profiles of the mean streamwise velocity at the inlet. Line colors defined in Table 1.

A no-slip condition is employed at the bottom wall while a free-slip condition is employed at the top boundary. Free-slip conditions are also used at the lateral boundaries and convective conditions are employed at the exit boundary. In two of the simulations the inflow conditions are time-independent and no turbulence is added to them. In these two cases, a Blasius profile is imposed at the inflow plane. In Simulation S1,  $\delta/H = 1$  and in Simulation S2,  $\delta/H = 0.1$ . In Simulation S3, the approaching boundary layer is turbulent. The mean inflow profile corresponds to one of the cases reported in Spalart [1988]. As in García-Villalba et al. [2009], the time-dependent inflow conditions are obtained by performing simultaneously a separate periodic LES of channel flow in which the mean velocity is forced to assume the desired vertical distribution using a body-force technique Pierce [2001]. By using this technique, the distribution of turbulent stresses obtained at the inflow plane is very similar to the standard distribution Spalart [1988] in a fully developed turbulent boundary layer. In this precursor calculation, the number of cells in streamwise direction is 72. The cost of this simulation is, therefore, 1/8 of the total cost. The three inflow profiles are shown in Fig. 1 (in the case of Simulation S3 the mean inflow profile is shown). The Reynolds number of the incoming boundary layer based on the momentum thickness,  $Re_\theta$ , for the three cases is also provided in Table 1.

### 3 Results

After discarding initial transients, statistics have been collected for a time span of roughly  $250 H/U_{ref}$ . This corresponds approximately to 11 flow-through times of the computational domain.

### 3.1 Pressure distribution

The mean drag coefficient of the hill,  $C_D = D/(0.5\rho U_{ref}^2 S)$ , where  $D$  is the drag including pressure and viscous terms,  $\rho$  is the fluid density, and  $S$  is the frontal surface, is reported in Table 1 for the three cases. Note that using the free stream velocity  $U$  in the definition of  $C_D$  might not be ideal in the present case because of the different amounts of momentum present in the incoming flow for  $y/H < 1$  (Fig. 1). The most important contribution to the drag is due to the pressure force on the surface. As an example, the pressure force is responsible for 91% of the drag in case S3. Similar values are obtained in the other two cases.

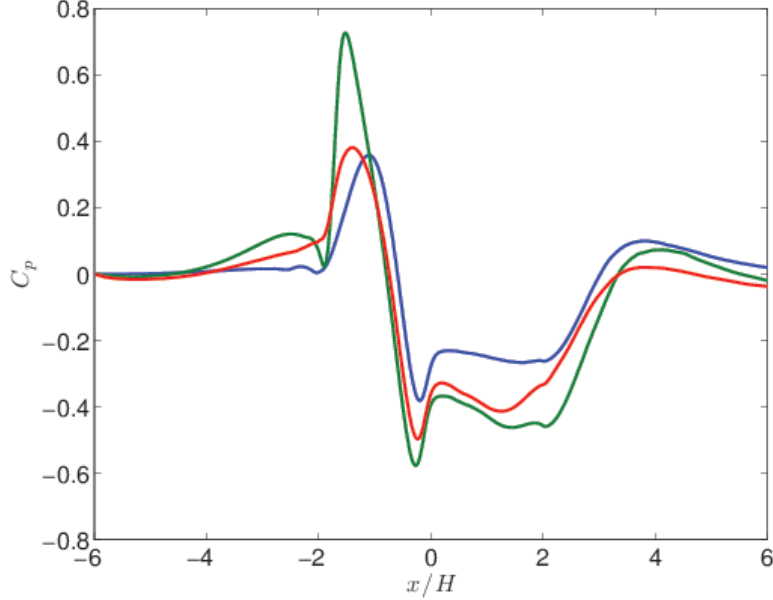


Figure 2: Pressure coefficient on the bottom surface along the centreline as a function of the streamwise coordinate. Line colors defined in Table 1.

Profiles of the pressure coefficient  $C_p = (p - p_\infty)/(0.5\rho U_{ref}^2)$  along the hill centreline are shown in Fig. 2. A similar trend is observed in the three cases. Upstream of the hill the pressure coefficient increases as the hill is approached, reaching a local maximum shortly after the windward slope of the hill starts. The maximum is more pronounced in case S2, which is the case in which more momentum is present below  $y/H = 1$  (Fig. 1). As a consequence, this is the case with the highest drag coefficient of the three. Thereafter, the flow accelerates and the pressure drops significantly reaching a local minimum near the top of the hill. Further downstream, the flow decelerates and the pressure recovers somewhat but due to the adverse pressure gradient the flow separates soon, producing a typical plateau in the profile of  $C_p$  upto  $x/H \sim 2.5$ . The peak pressure at reattachment occurs around  $x/H \sim 4$  in all cases.

### 3.2 Mean flow topology

Closely connected with the pressure distribution is the mean flow topology map displayed in Fig 3. This figure shows streamlines of the mean flow projected onto a wall-parallel surface at a distance to the wall of  $y/H = 0.01$ . In addition, the blue patches indicate the region where backflow is present ( $U < 0$ ). The overall pattern is similar in all three cases but a few differences are observed.

A total of eight topological features can be observed in all cases (see Fig. 3d for case S3). Four saddle points, which are all located along the centreline, and four nodes, two located on the centreline, and two foci, located on both sides of the hill, around  $x/H \sim 1.5$ ,  $z/H \sim \pm 0.5$ . As expected, these

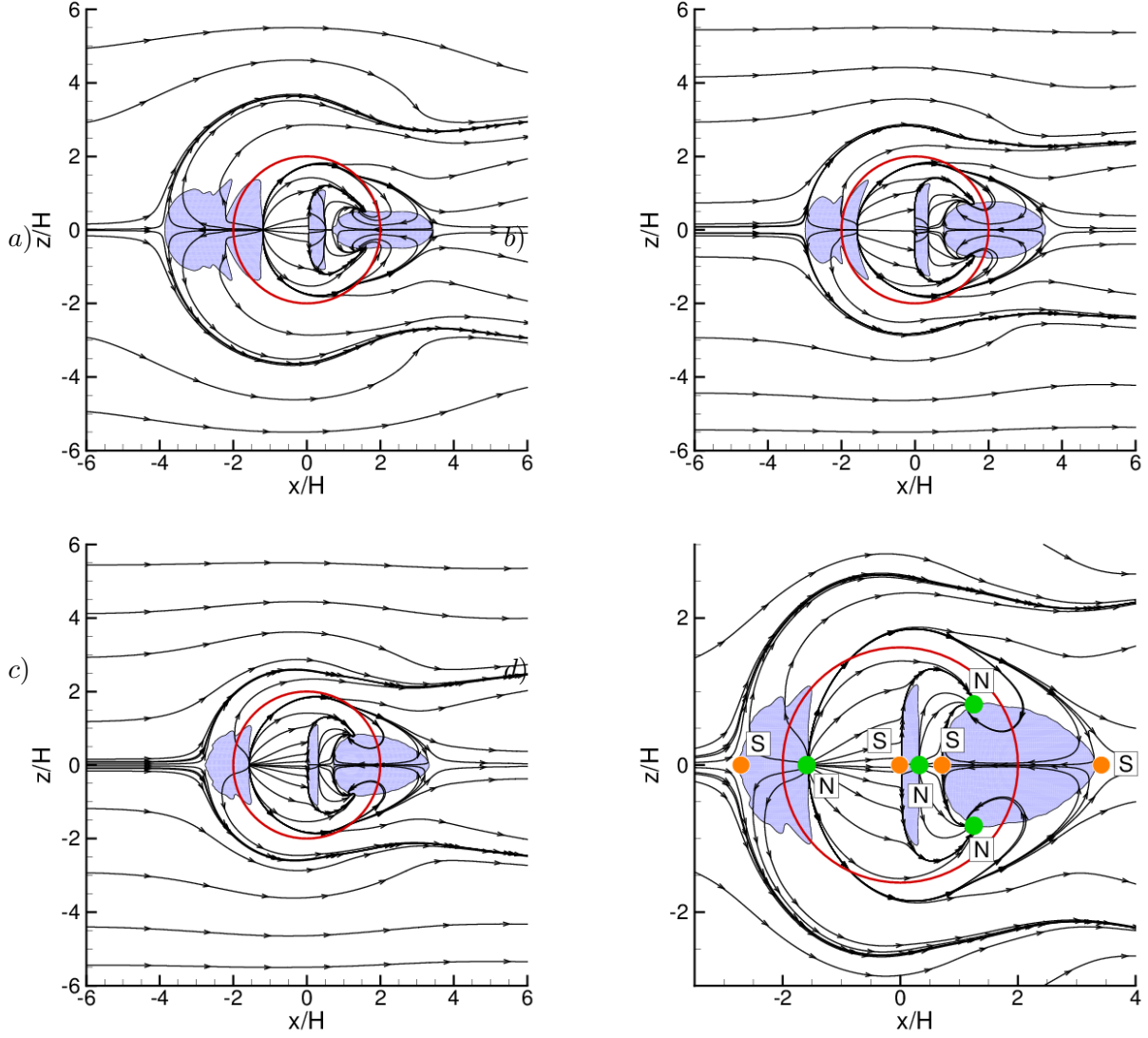


Figure 3: Streamlines of the mean flow projected onto a wall-parallel surface at a distance to the wall  $y/H = 0.01$ . The blue patches indicate the region where backflow is present  $U < 0$ . a) S1. b) S2. c) S3. d) Zoom of S3 identifying saddles (orange) and nodal points (green).

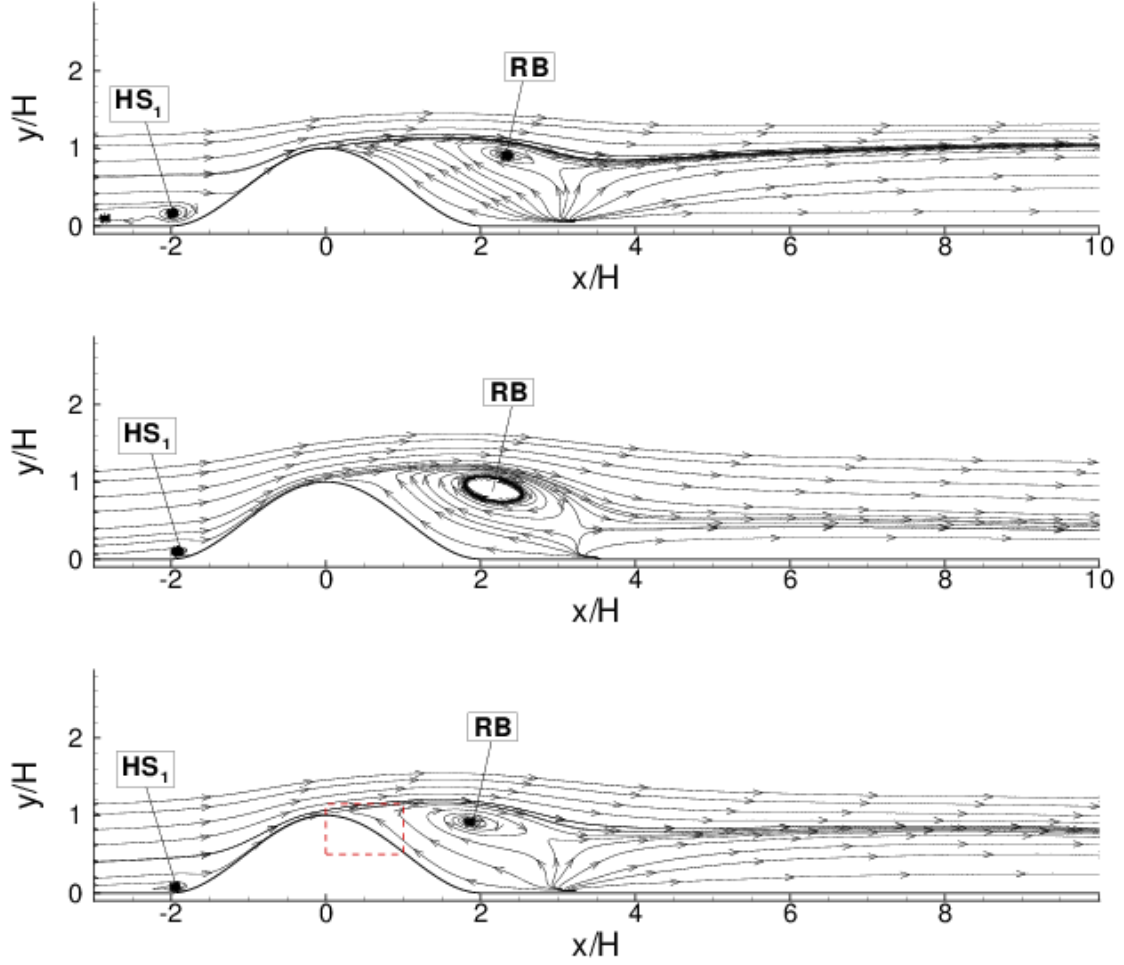


Figure 4: Streamlines of the mean flow in the midplane. Top, S1. Middle, S2. Bottom, S3. The red square identifies the zoomed-in region shown in Fig. 5

topological features satisfy the conditions provided by Hunt et al. [1978] for flow over obstacles (same number of saddle and nodal points).

In all cases, there are two main areas of backflow, one in the windward part of the hill and a second one in the rear part. The backflow in the windward part of the hill is located between a saddle point and a nodal point on the centreline. The appearance of this region is related to a well-known phenomenon in the flow around wall-mounted obstacles: the formation of a horseshoe vortex at the foot of the obstacle. This has been observed in flow over wall-mounted cubes, cylinders, etc. However, this is not observed for the present geometry at significantly higher Reynolds numbers García-Villalba et al. [2009]. It is noticeable that this region is largest in Simulation S1, while in S2 and S3 the smaller regions are of comparable size. The streamlines arriving at the first saddle point from upstream, are deviated to both sides to go around the hill. In the Simulation S1 they are deviated as far as  $|z/H| \sim 4$  while in S2 and S3 they remain within  $|z/H| \sim 3$ .

The backflow region in the rear part has a more complex structure. It is split in two parts with a forward flow region in between. It turns out that this forward flow region is extremely thin (as discussed below), this is why we refer to the rear backflow region as a single region. The differences between the three simulations are minor. The location of saddle and nodal points are approximately the same in all cases and therefore the topology of the streamlines that connect them is the same.

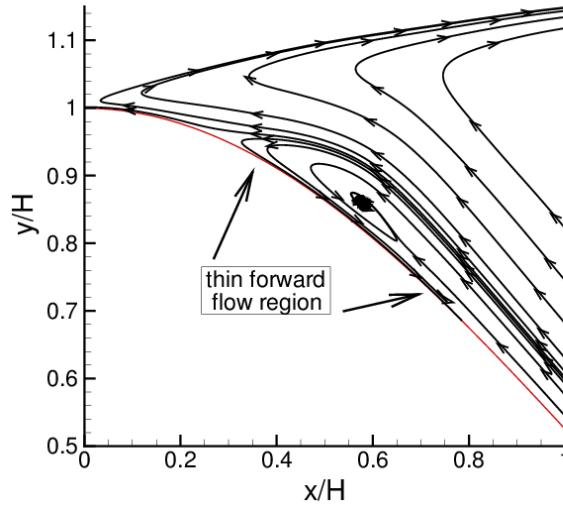


Figure 5: Streamlines of the mean flow in the midplane (Zoomed view). Simulation S3.

### 3.3 Mean velocity distribution

Figure 4 shows a comparison of streamlines of the mean flow in the symmetry plane of Simulations S1, S2 and S3. The main recirculation region behind the hill is longer and higher than the one observed for this same geometry at a significantly higher Reynolds number García-Villalba et al. [2009]. The centre of the main recirculation bubble behind the crest of the hill is identified by the label  $RB$ . While  $HS_1$  identifies the small upstream area of recirculation (vortex) obtained at the foot of the hill. Because of the strong accelerating mean flow along the foot of the hill, the upstream vortex  $HS_1$  is stretched in the streamwise direction. As it is wrapped partially around the foot of the hill the horse shoe vortex mentioned above is formed. The shape of the horse shoe vortex is reflected in the lateral streamlines that originate from the upstream saddle point, shown in Figure 3. Because of the larger  $Re_\theta$  (Tab. 1) of the incoming (laminar) boundary layer, compared to Simulations S2 and S3, in Simulation S1 a significantly larger upstream separation bubble  $HS_1$  is generated. Also, the streamlines - originating from the crest of the hill - that bound the wake-like wall-parallel flow show that the height of the wake increases with increasing  $Re_\theta$  of the inflow profile (see Table 1).

Below the main recirculation region, a very shallow secondary bubble is obtained in all three simulations. Evidence of this can be seen in Fig. 3. However, this bubble is not visible in Fig. 4. A zoomed view of simulation S3, presented in Fig. 5, illustrates the shape of the secondary bubble. This thin region is resolved in the simulation with 8 to 10 grid points in wall-normal direction.

Figure 6 shows the streamwise velocity profiles of the three simulations at  $x/H = -4, -2, 2, 5, 8, 11$ . At  $x/H = -2$  the profiles confirm the presence of the separation bubble  $HS_1$  at the foot of the hill in all simulations. The presence of the main recirculation bubble  $RB$  is clearly reflected in all three simulations by the reverse flow in the profiles shown at  $x/H = 2$ . Despite the difference in the profiles and the state (laminar/turbulent) of the flow at the inflow plane, for  $x/H = 2, \dots, 11$  the mean profiles of all three simulations do not present significant differences. Furthermore, the profiles for  $x/H = 5, 8, 11$  all exhibit the characteristic full turbulent boundary layer profile at the bottom with a wake-like region on top.

Figure 7 shows a comparison of the mean  $u$ -velocity profiles at various stations  $z/H = 0, 1, 2, 3$  and 4, extracted in the cross section at  $x/H = 5$ . While at the symmetry plane ( $z/H = 0$ ) the velocity profiles almost collapse, towards the edges of the computational domain gradually more and more

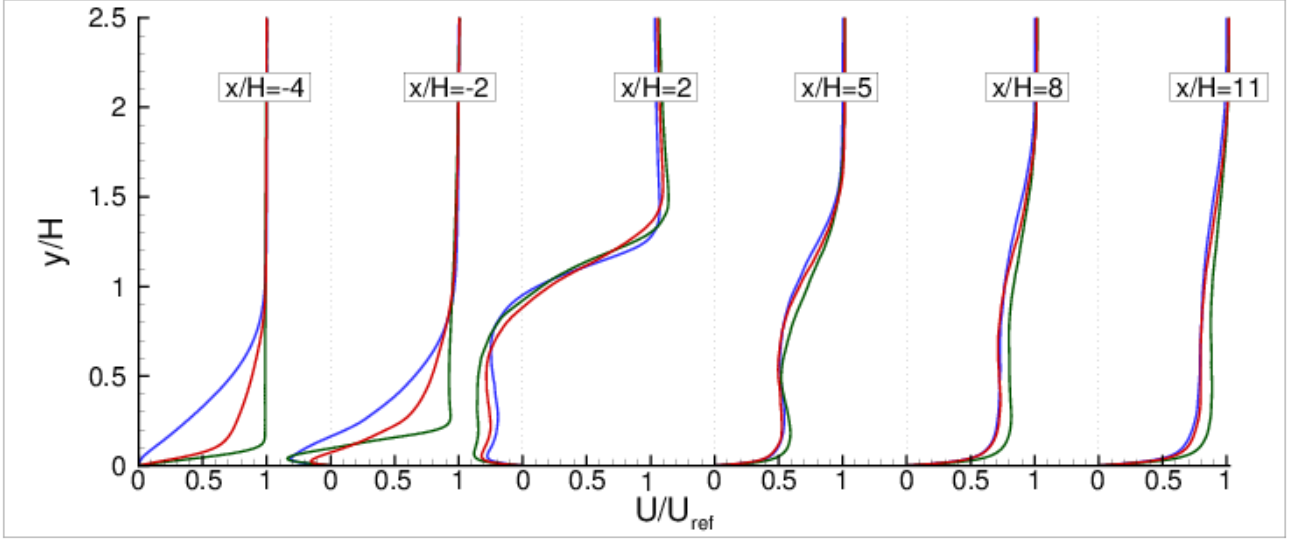


Figure 6: Profiles of mean streamwise velocity in the midplane  $z/H = 0$ , at various streamwise locations:  $x/H = -4, -2, 2, 5, 8, 11$ . Line colors defined in Table 1.

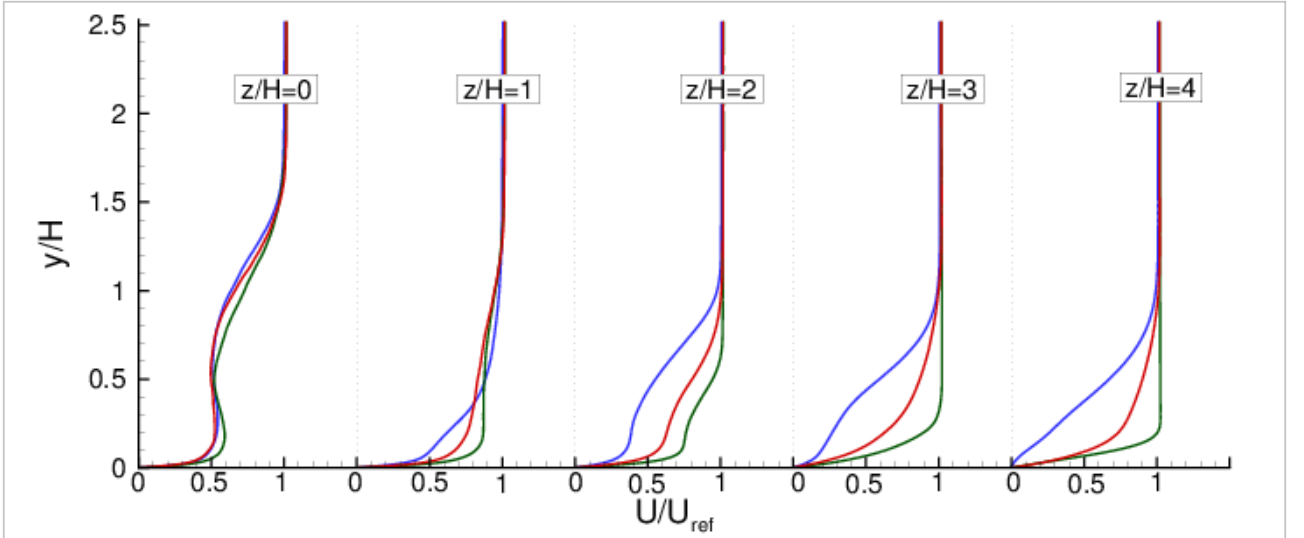


Figure 7: Profiles of mean streamwise velocity at  $x/H = 5$ , at various spanwise locations:  $z/H = 0, 1, 2, 3, 4$ . Line colors defined in Table 1.

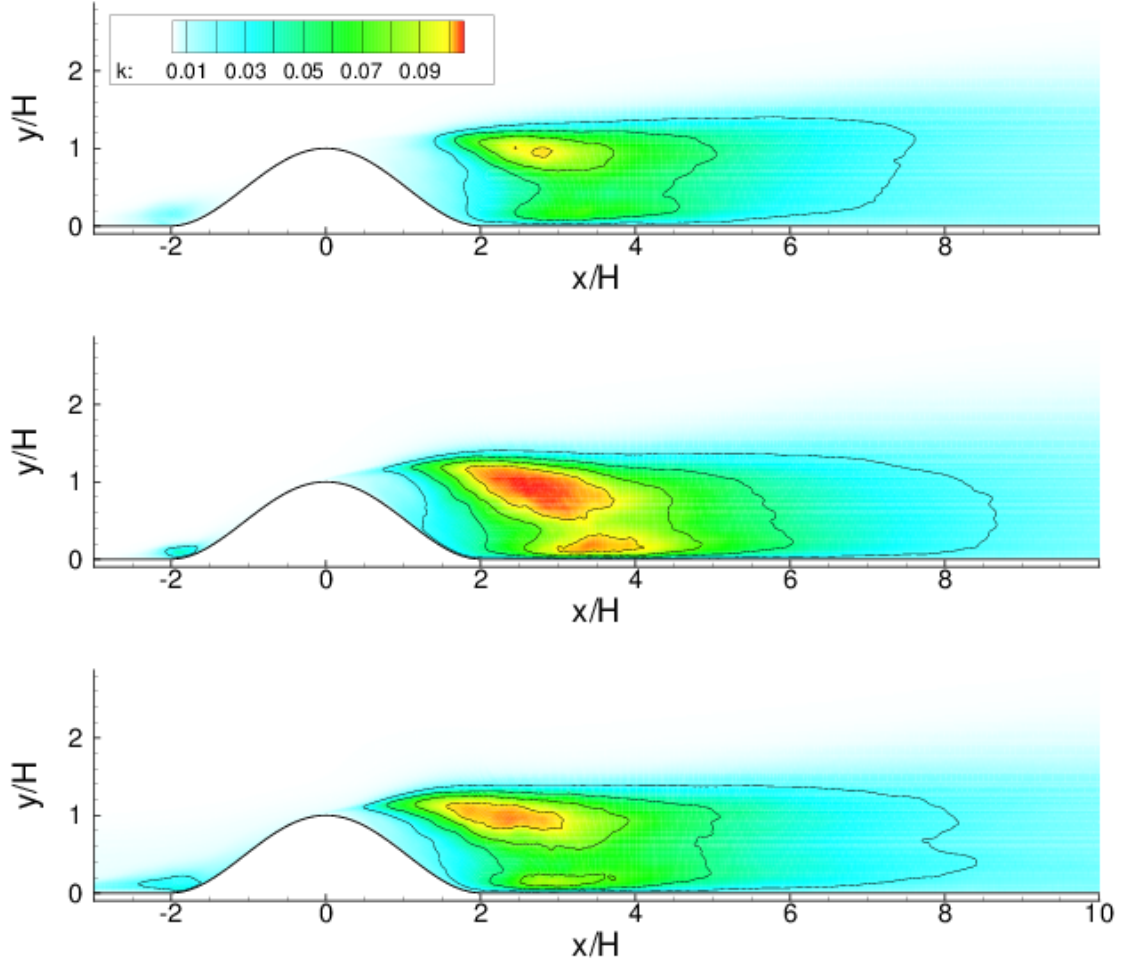


Figure 8: Contours of turbulent kinetic energy in the midplane. Top, S1. Middle, S2. Bottom, S3. Lines are  $k/U_{ref}^2 = 0.025, 0.05, 0.075$  and  $0.1$ .

differences can be observed. At  $z/H = 4$ , finally, for each simulation the shape of the mean  $u$ -velocity profile is found to be very similar to the mean inflow velocity profile. Hence, the downstream influence of the hill (in the form of a wake) is only noticeable in a spanwise region of limited size.

### 3.4 Turbulence in the symmetry plane

Figure 8 shows the turbulent kinetic energy,  $k$ , in the symmetry plane for Simulations S1, S2 and S3. Immediately upstream of the hill, at  $x/H \approx -2$ , in each simulation a small patch with an elevated  $k$ -level can be observed that coincides with the upstream separation bubble labelled  $HS_1$  in Figure 4. The production of kinetic energy leading to increased values of  $k$  in the re-circulation zone of a separation bubble was observed earlier in Wissink [2003], Wissink et al. [2006] and was accounted for by an elliptic instability of the rolled-up shear layer. Downstream of the small separation bubble, the streamwise pressure gradient turns favourable and the energized boundary layers in all simulations re-attach. Also, at the centre of the circulation bubble, downstream of the crest of the hill - labelled  $RB$  in Figure 4 - production of kinetic energy is observed in all simulations. Of the three simulations, the momentum thickness of the incoming boundary layer in Simulation S2 is smallest, followed by Simulation S3 and then Simulation S1. Because of this, in the inflow region the wall-shear

in Simulation B is significantly larger than in Simulations S1 and S2. As the boundary layer separates from the crest of the hill, the mean shear in the free-shear layers generates turbulence. Because in Simulation S2 the mean shear is much stronger than in Simulations S1 and S3, the production of  $k$  in Simulation S2 is significantly higher (as confirmed in Figure 8). Similarly, because of the difference in wall-shear strength, in Simulation S1 the production of  $k$  is found to be lower than in Simulation S3.

Profiles of the rms values of the  $u$ -,  $v$ - and  $w$ -velocity components of the three simulations are shown in Figure 9. Close to the inflow plane, at  $x/H = -4$ , the rms-values of all velocity components of the two Simulations S1 and S2 are observed to be zero. In the upstream separation bubble,  $HS_1$ , at  $x/H = -2$ , all three velocity components exhibit fluctuations as reflected by the locally increased rms-values. On the lee side of the hill, at  $x/H = 2$ , the presence of the large recirculation bubble  $RB$  induces significant fluctuations in all simulations. Because of the increased momentum thickness of Simulation S1's incoming boundary layer, the fluctuation in the rms-values is found to be slightly less than in Simulations S2 and S3. For  $x/H \geq 5$ , the profiles of the rms values of the velocity components become similar, indicating that the significant differences in the shape and state (laminar/turbulent) of the boundary layers at the inflow plane is no longer identifiable by studying differences in the rms values in the symmetry plane. Compared to the Simulations S1 and S3, the only significant difference is observed in the  $w_{rms}$  values of Simulation S2 at  $x/H = 5$  which, close to the lower wall, are significantly higher than in Simulations S1 and S3. This is likely related to the increased mass flux in Simulation S2.

### 3.5 Secondary motions

In the wake of the hill, the boundary layer recovers with a combination of streamwise acceleration (Fig. 6) and transverse (secondary) circulation. The secondary motion is relatively weak with a peak velocity around 10-15% of  $U_{ref}$  and it originates from the realignment of the vorticity generated upstream of the hill (horseshoe vortex) and additional vorticity shed from the surface of the hill. The vorticity generation at the wall and its subsequent re-orientation is discussed in §3.6. Fig. 10 shows the streamwise evolution of the secondary motion at three locations in the near wake of the hill, namely  $x/H = 1, 2$  and  $5$ .

At  $x/H = 1$ , the legs of the horseshoe vortex are clearly visible around  $|z/H| \sim 2$ . It is interesting to note that in Simulation S1 two vortices ( $|z/H| \sim 2$  and  $|z/H| \sim 2.8$ ) are present with a counter-rotating region in between. On the other hand, in Simulations S2 and S3 only one such vortex is visible. Further downstream for these two simulations there is a trace of a second vortex (labeled  $HS_2$ ) although much weaker than in Simulation S1.

At  $x/H = 2$ , a secondary vortex labelled HP appears in all three simulations at  $|z/H| < 1$ . Further downstream, at  $x/H = 5$ , for Simulations S1 and S3 this vortex remains present, with the eye slightly displaced upwards. In Simulation S2, this secondary vortex seems to have collapsed in the midplane.

Contours of turbulent kinetic energy  $k$  are also included in Fig. 10. The development of the turbulent kinetic energy in the wake occurs at a later streamwise position in Simulation S1 compared to Simulations S2 and S3. At  $x/H = 1$  patches of  $k$  can be observed in the region  $|z/H| < 1$  in Simulations S2 and S3, but not in Simulation S1 (see also Fig. 8). At  $x/H = 2$ , the peak of  $k$  is stronger in Simulations S2 and S3. The turbulent kinetic energy is concentrated in the shear layer between the free stream and the recirculation region, in all three simulations. Additionally, there is a patch further outwards, which is related to the recirculation in the horseshoe vortex. Further downstream, at  $x/H = 5$ , the decay of  $k$  with respect to the previous location is clearly visible, a typical phenomenon of wakes. In order to illustrate in a more quantitative manner the differences between the three simulations at this streamwise location ( $x/H = 5$ ), vertical profiles of  $k$  at various spanwise locations are shown in Fig. 11. At the midplane ( $z/H = 0$ ),  $k$  is largest in Simulation S2, by a factor of about 20%, while Simulations S1 and S3 present similar values. At  $z/H = 1$ ,  $k$  of Simulation S1 has decreased significantly compared to Simulation S3, indicating that the width of the

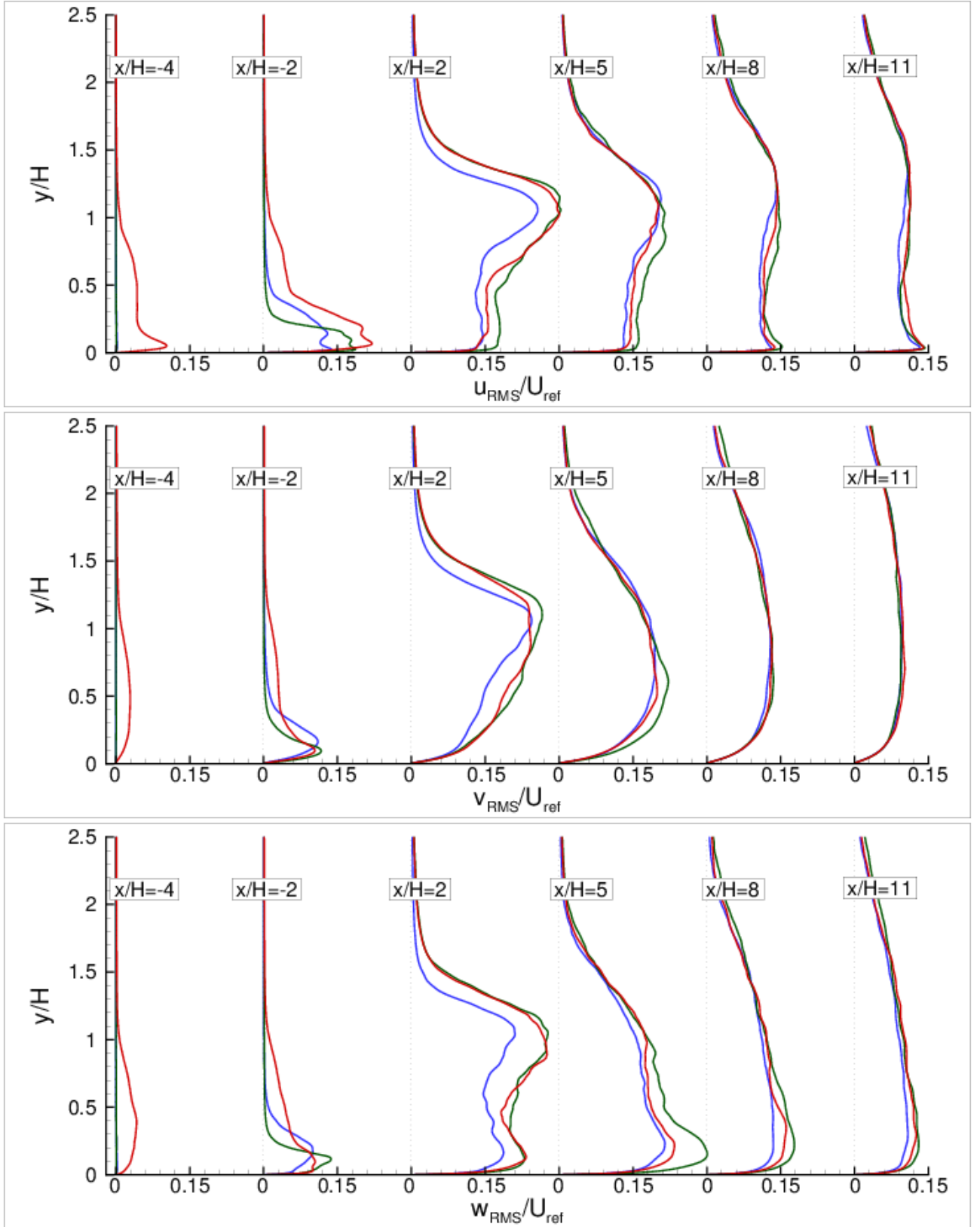


Figure 9: Profiles of rms-velocity components in the midplane  $z/H = 0$ , at various streamwise locations:  $x/H = -4, -2, 2, 5, 8, 11$ . Top, streamwise velocity  $u_{rms}/U_{ref}$ . Middle, vertical velocity  $v_{rms}/U_{ref}$ . Bottom, spanwise velocity  $w_{rms}/U_{ref}$ . Line colors defined in Table 1.

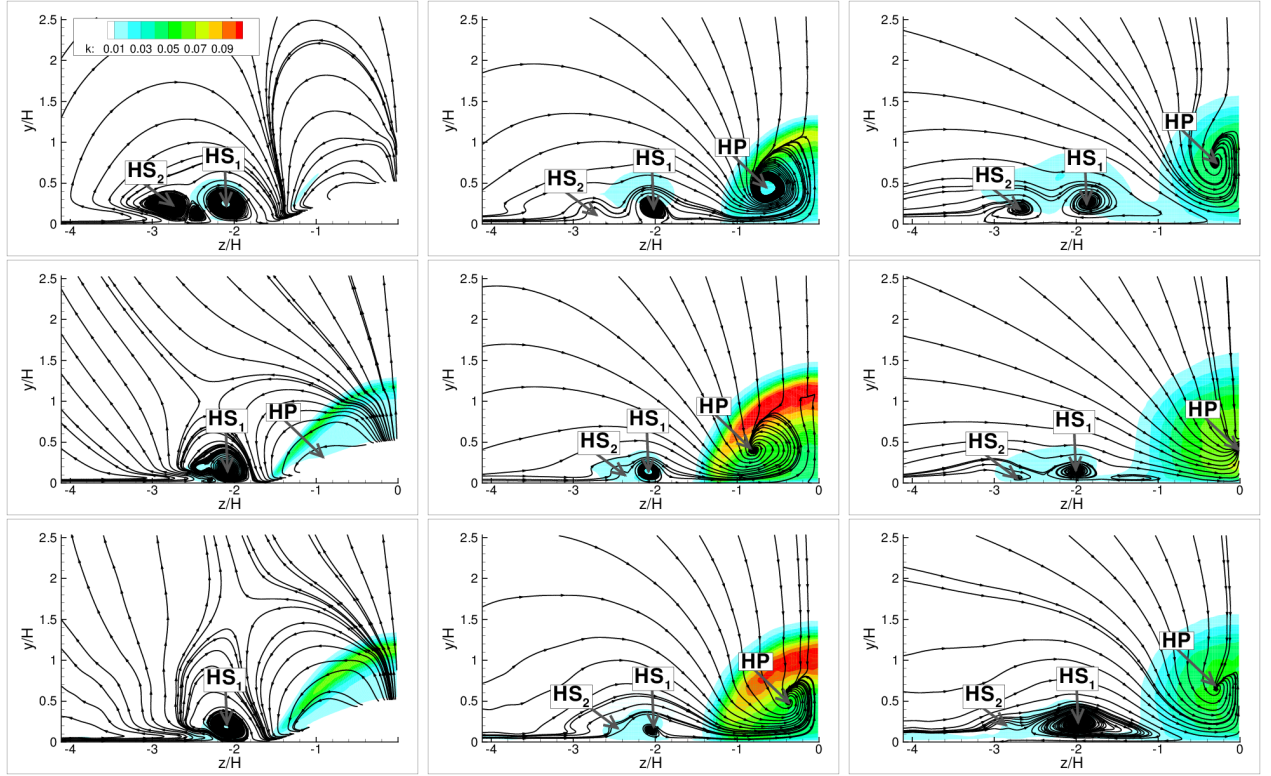


Figure 10: Secondary motions. Top, S1. Middle, S2. Bottom, S3. Left column,  $x/H = 1$ . Middle column,  $x/H = 2$ . Right column,  $x/H = 5$ . Color represents turbulent kinetic energy.

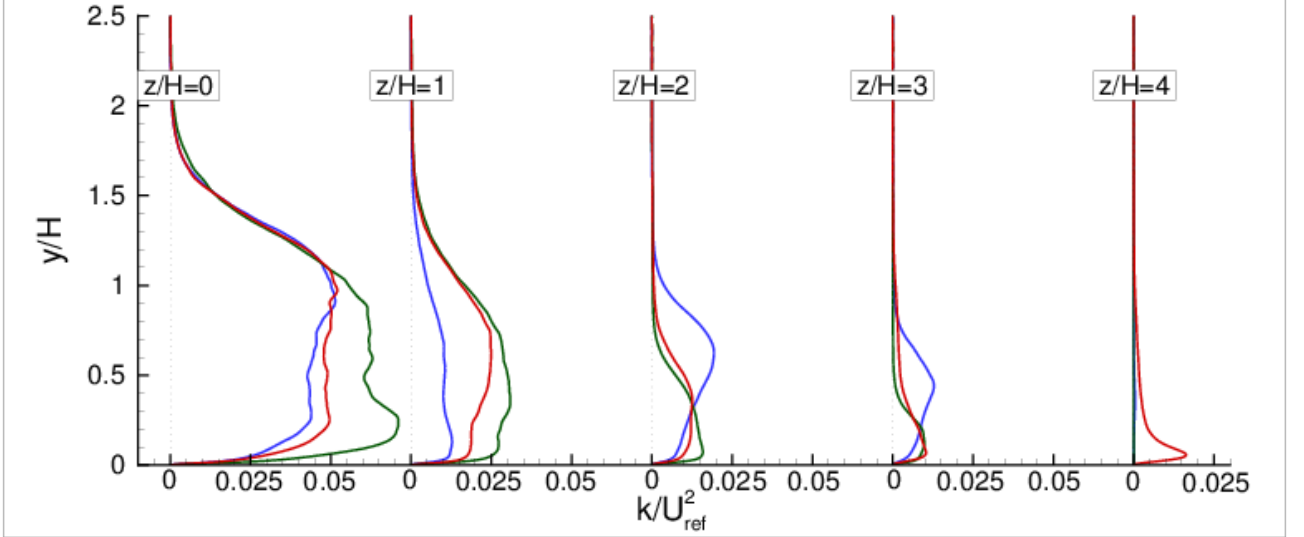


Figure 11: Profiles of turbulent kinetic energy at  $x/H = 5$ , at various spanwise locations:  $z/H = 0, 1, 2, 3, 4$ . Line colors defined in Table 1.

wake is smaller in Simulation S1. Further outwards, at  $z/H = 2$  and  $3$ ,  $k$  of Simulation S1 presents larger values than Simulations S2 and S3, and in particular at larger heights. This indicates that the horseshoe vortex is strongest in Simulation S1 and transition to turbulence happens later. Finally, at  $z/H = 4$ , all simulations have recovered the values specified at the inlet, S1 and S2 are laminar while S3 is turbulent. Therefore, at this location the boundary layer is undisturbed by the hill.

### 3.6 Vorticity flux

Vorticity production at a solid boundary can be described in terms of vorticity flux. For three-dimensional flows, the mean vorticity flux can be defined Panton [1984], Andreopoulos and Agui [1986] as

$$\vec{\sigma} = -\nu(\mathbf{n} \cdot \nabla \vec{\omega})_w, \quad (2)$$

where  $\vec{\sigma}$  is the mean vorticity-flux vector,  $\vec{n}$  is the normal vector to the surface, towards the fluid and  $\vec{\omega}$  is the mean vorticity vector.

As an illustration, Fig. 12 displays the three components of the mean vorticity flux at the wall from case S2 (the distributions of the other two cases are similar). There is production of spanwise vorticity everywhere in the flow, while the production of vertical and streamwise vorticity is concentrated in the hill region. Obviously, in the absence of the hill,  $\omega_x$  and  $\omega_y$  would be zero. In the vicinity of the hill,  $\sigma_z$  (Fig. 12c) reverses sign as a consequence of the reverse flow which occurs both upstream and downstream of the hill. The negative vorticity flux peaks in the region where the flow strongly accelerates. Production of  $\omega_y$  occurs when the oncoming flow is deviated sideways to pass along the left and the right of the hill (only the deviation to the right is illustrated). On the half-domain displayed in Fig. 12b, only negative  $\omega_y$  is generated. Finally, production of  $\omega_x$  (Fig. 12a) is concentrated towards the side of the hill: Negative  $\omega_x$  is generated upstream of the crest due to the flow moving upwards and to the right, while downstream of the crest positive  $\omega_x$  is generated due to the flow moving downwards and to the left.

It is interesting to compare the magnitude of the mean vorticity flux  $\sigma = \sqrt{\sigma_i \sigma_i}$  for the three cases. This is done in Fig. 13. Away from the hill, the values of  $\sigma$  are higher in cases S2 and S3 compared to S1. This is due to the much lower wall-shear in case S1 (see Fig. 1). In the hill region, the maximum values of  $\sigma$  are of the same order in all cases ( $\sigma \sim 3U_{ref}^2/H$ ). These high values are

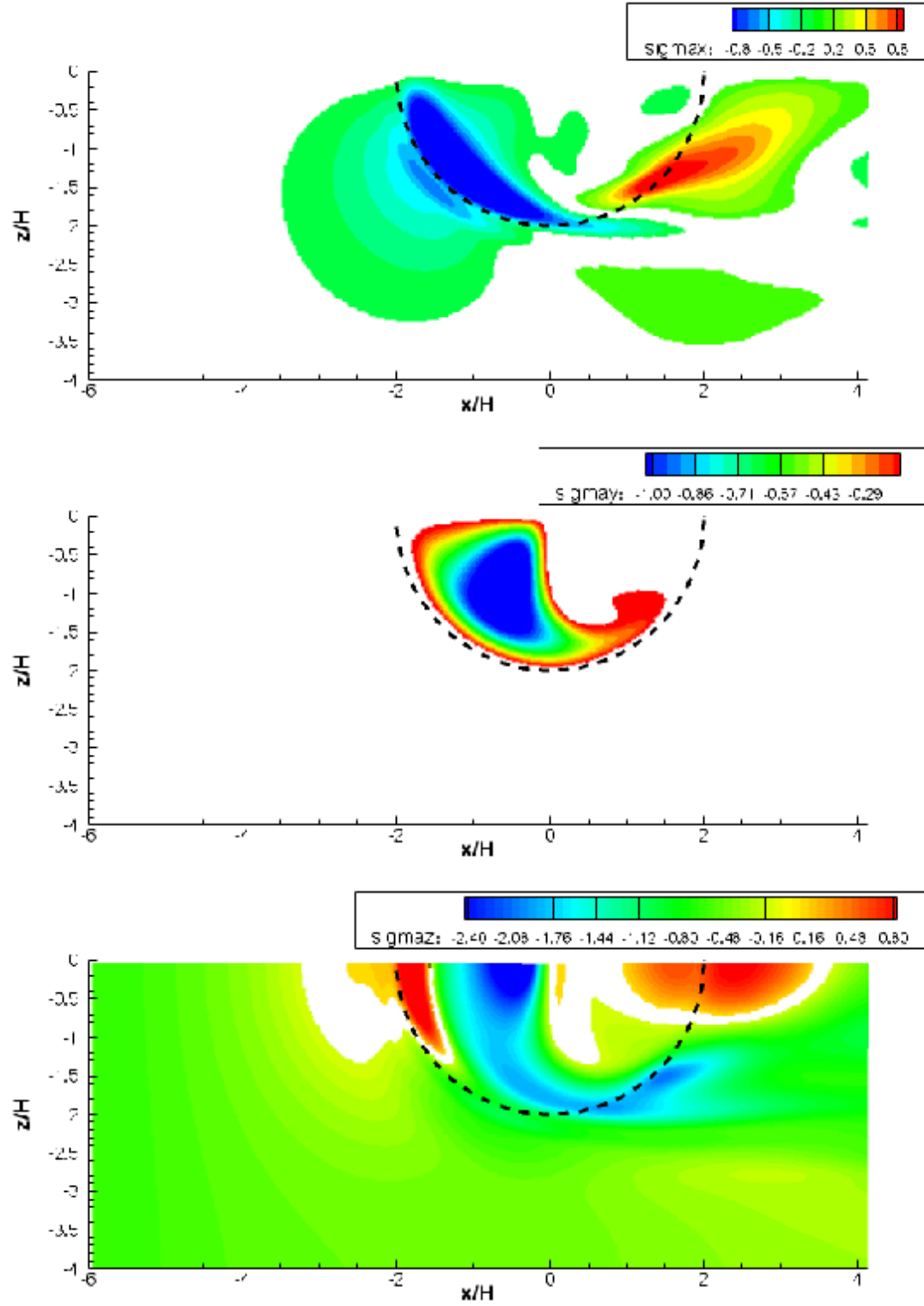


Figure 12: Components of the mean vorticity flux at the wall, case S2. Blanking has been used for  $|\sigma| < 0.1$  Top,  $\sigma_x$ . Middle,  $\sigma_y$ . Bottom,  $\sigma_z$ .

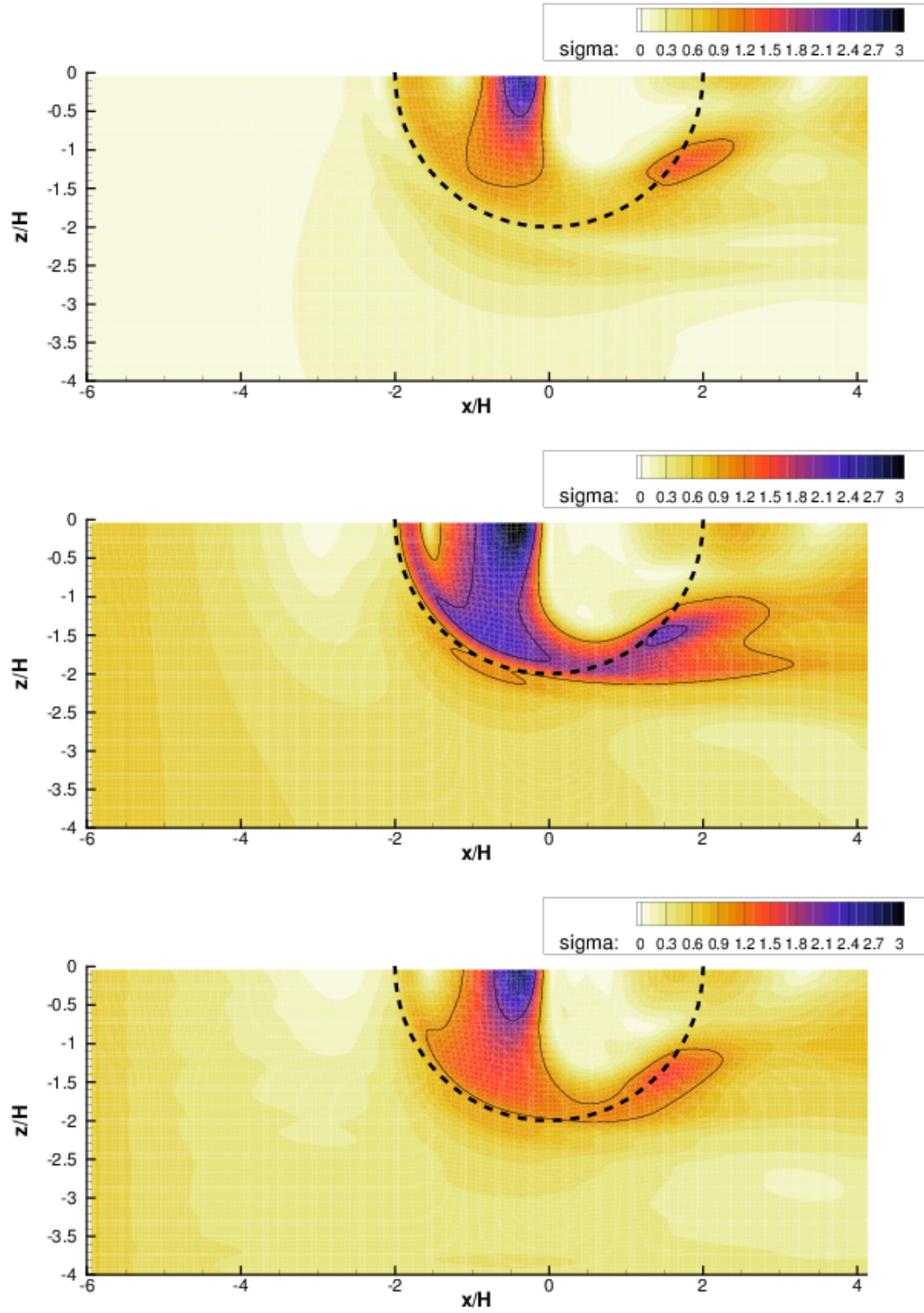


Figure 13: Magnitude of the mean vorticity flux at the wall. Top, S1. Middle, S2. Bottom, S3.

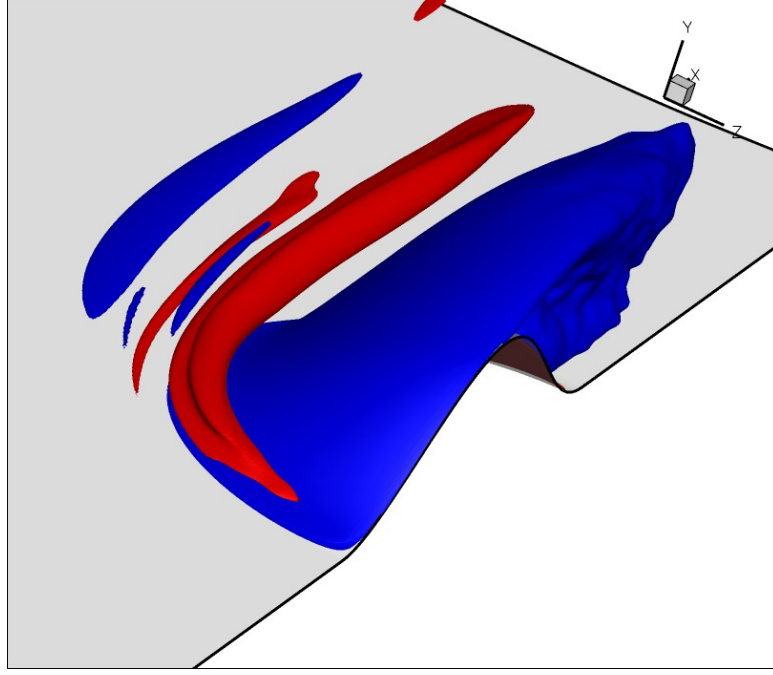


Figure 14: Iso-surfaces of mean vertical vorticity from S2. Blue,  $\omega_y = -0.5$ . Red,  $\omega_y = 0.5$ .

attained just upstream of the top: in the region of strong acceleration of the streamwise velocity (which leads to production of  $\omega_z$ ), and towards the sides: where the flow is deviated to the left and to the right (which leads to production of  $\omega_x$  and  $\omega_y$ ). It can be seen that, while in all three cases similarly shaped contours are obtained, case S2 has the highest flux, followed by S3 and, finally, S1. The reason for this is that in S2 more momentum is present below  $y/H = 1$  (Fig. 1), than in S3, while S3 has more momentum below  $y/H = 1$  than S1. The trend (and the argument) is the same as for the pressure coefficient discussed above. By comparing  $\sigma$  in the region of the hill ( $\sigma_H$ ) to its value at the inflow ( $\sigma_0$ ), it is possible to quantify the relative influence of the upstream vorticity and the vorticity generated over the hill. Due to the low  $\sigma_0$  in case S1,  $\sigma_H/\sigma_0$  reaches values as high as 50, while in the other two cases this ratio is lower;  $\sigma_H/\sigma_0 \sim 8$  in S2 and  $\sigma_H/\sigma_0 \sim 6$  in S3.

After being produced at the wall, vorticity is subsequently convected and re-oriented by the mean flow. This is illustrated in Fig. 14, which displays iso-surfaces of the vertical vorticity for case S2. Because similar features are observed in the other two cases, we limit the discussion to S2. Fig. 12b shows that, for the region considered, only negative  $\omega_y$  is produced at the wall. The blue iso-surface  $\omega_y = -0.5U_{ref}/H$  originates exactly in the region of production and is then convected into the wake. The red iso-surface  $\omega_y = 0.5U_{ref}/H$  is, however, not produced at the wall. Instead, this region corresponds to the horseshoe vortex and is formed through re-orientation of spanwise vorticity from the incoming boundary layer. Fig. 15 displays the values of  $\omega_x$  and  $\omega_y$  in the wake of the hill. These two components, which are generated as the flow passes over and around the hill, can be seen to be gradually dissipated in the downstream direction. The vanishing non-spanwise mean vorticity indicates that, with increasing distance from the hill, the wake-flow is becoming more and more homogeneous in the spanwise direction. This figure is related to the secondary motions that were displayed in Fig. 10. In particular, the patches of  $\omega_x$  and  $\omega_y$ , which are located in the region  $|z/H| \lesssim 1$ , are related to the secondary vortex labelled HP in Fig. 10. The outer patches are related to the horse-shoe vortex labelled HS1 and HS2 in the same figure. Therefore, we can conclude that the secondary vortex HP is a direct consequence of the vorticity production at the surface of the hill while the horse-shoe vortices HS1 and HS2 are only indirectly generated by the hill through re-orientation

of vorticity.

### 3.7 Instantaneous flow

A visualization of the instantaneous coherent structures of the flow is displayed in Fig. 16. The figure (and corresponding animations) shows an iso-surface of pressure fluctuations for the value  $p - \langle p \rangle = -0.02$ . This visualization technique has been often used in the past Fröhlich et al. [2005], García-Villalba et al. [2006]. Coherent structures are observed to form in the lee of the hill and are convected downstream. Many of them have the shape of a hairpin vortex. Similar structures have been also observed at high Reynolds number, although in that case, they were more irregular García-Villalba et al. [2009]. It is also well-known that at lower Reynolds number, a hemisphere protuberance in a laminar boundary layer generates a train of very regular hairpin vortices Acarlar and Smith [1987]. It was shown in the cited study that the behaviour of the wake was quite regular upto  $Re_H \sim 3400$ . Beyond that the shedding became irregular. The present investigation ( $Re_H = 6650$ ) lies already in the irregular regime.

An important difference with respect to the high Reynolds number case is the visibility of structures originating upstream of the hill at the reduced Reynolds number considered. These structures are secondary vortical structures that appear on top of the horseshoe vortex. In the present case, these hairpin vortices are more clearly visible in the cases with laminar inflow, in particular, in Simulation S1, see Fig. 16(top) and Animation S1. In the middle, a train of large hairpin vortices can be observed, while at both sides of the hill a sequence of much smaller hairpin vortices can be seen. In Simulations S2 and S3, (Fig. 16 middle and bottom, respectively) the large hairpin vortices in the middle can still be observed, but the smaller vortices at each side of the hill have become more difficult to identify (Simulation S2 and Animation S2) or almost completely vanished (Simulation S3 and Animation S3). It appears that the reduced wall-shear in Simulation S1 provides ideal conditions for the generation of a horseshoe vortex on which secondary vortical structures are formed that, in the downstream direction, turn into hairpin vortices. Note that the primary horseshoe vortex can only be indirectly detected by studying iso-surfaces of the pressure fluctuations. The turbulence, combined with the increased wall-shear stress in Simulation S3 virtually prevent the formation of secondary vortical structures on the horseshoe vortex.

## 4 Conclusions

In this paper, results of three LES of flow over and around a three-dimensional hill at moderate Reynolds numbers have been presented. The Reynolds number is lower than in previous investigations García-Villalba et al. [2009] and this has a significant impact in the wake region. While in the present investigation the flow is massively separated, leading to a large recirculation region behind the hill, at high  $Re$  the recirculation region is very shallow García-Villalba et al. [2009]. Therefore, no quantitative comparison with the previous case is reported in this paper. Two of the simulations have incoming laminar boundary layers of different thicknesses and the third one has an incoming turbulent boundary layer. It has been shown that the main features of the flow behind the hill are very similar in all three simulations. For instance, the similar size of the main recirculation bubble behind the hill, the presence of a horseshoe vortex originating immediately upstream of the hill, a similar wall-topology map and a virtual collapse of the mean streamwise velocity profiles in the midplane beyond  $x/H = 5$ . In spite of this, there are various differences which need to be pointed out: 1) The height of the wake, which increases with increasing  $Re_\theta$  of the inflow profile 2) The maximum level of kinetic energy in the wake varies from 20% to 30% depending on the simulation. 3) The horseshoe vortex is observed to be significantly affected by the inflow characteristics. 4) The main secondary motion in the central region is found to be quite sensitive to the actual inflow condition prescribed, which might have a significant impact on heat and mass transport. 5) The instantaneous coherent structures show

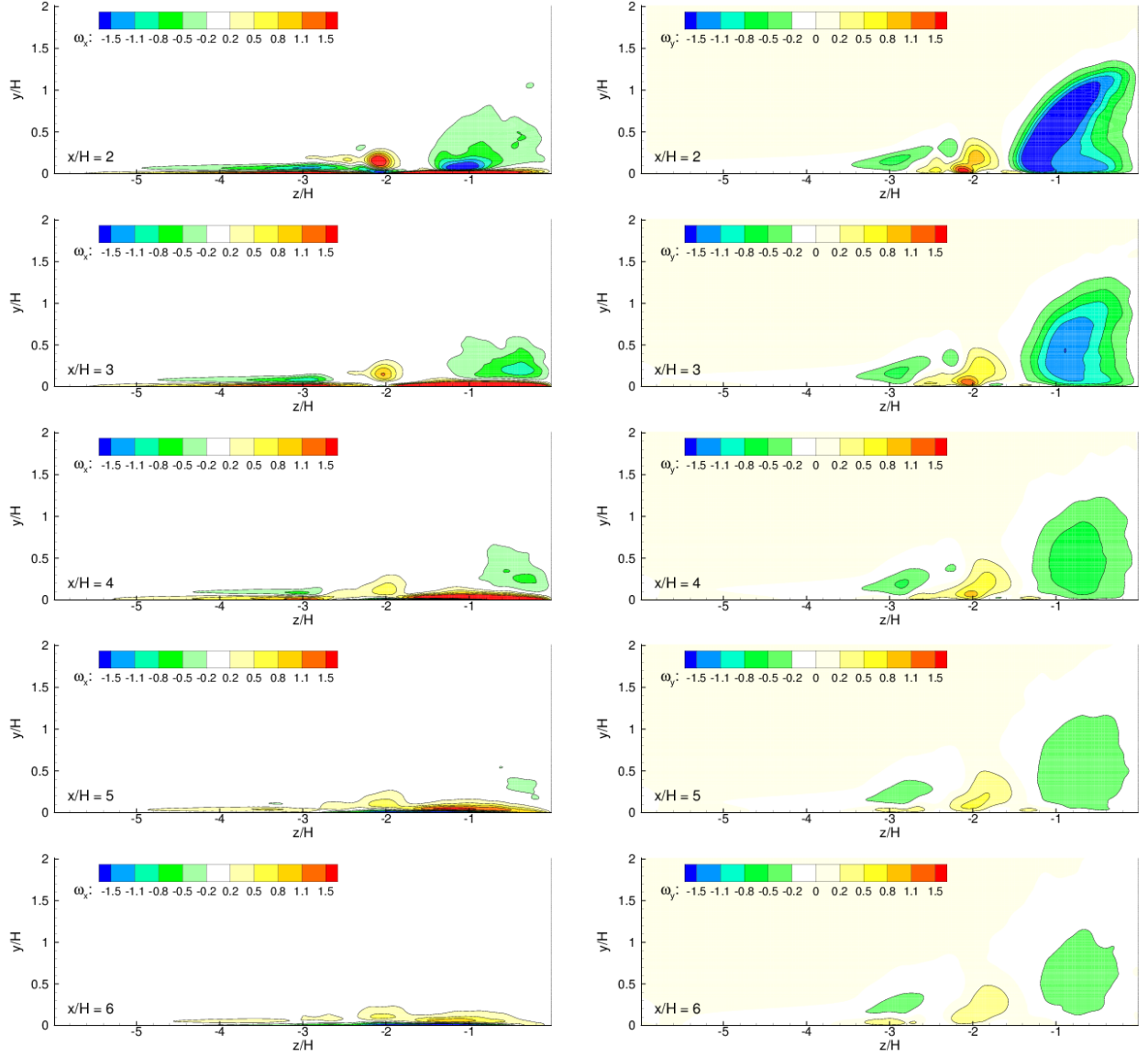


Figure 15: Contours of mean streamwise (left) and vertical (right) vorticity from S2. From top to bottom,  $x/H = 2, 3, 4, 5$  and 6.

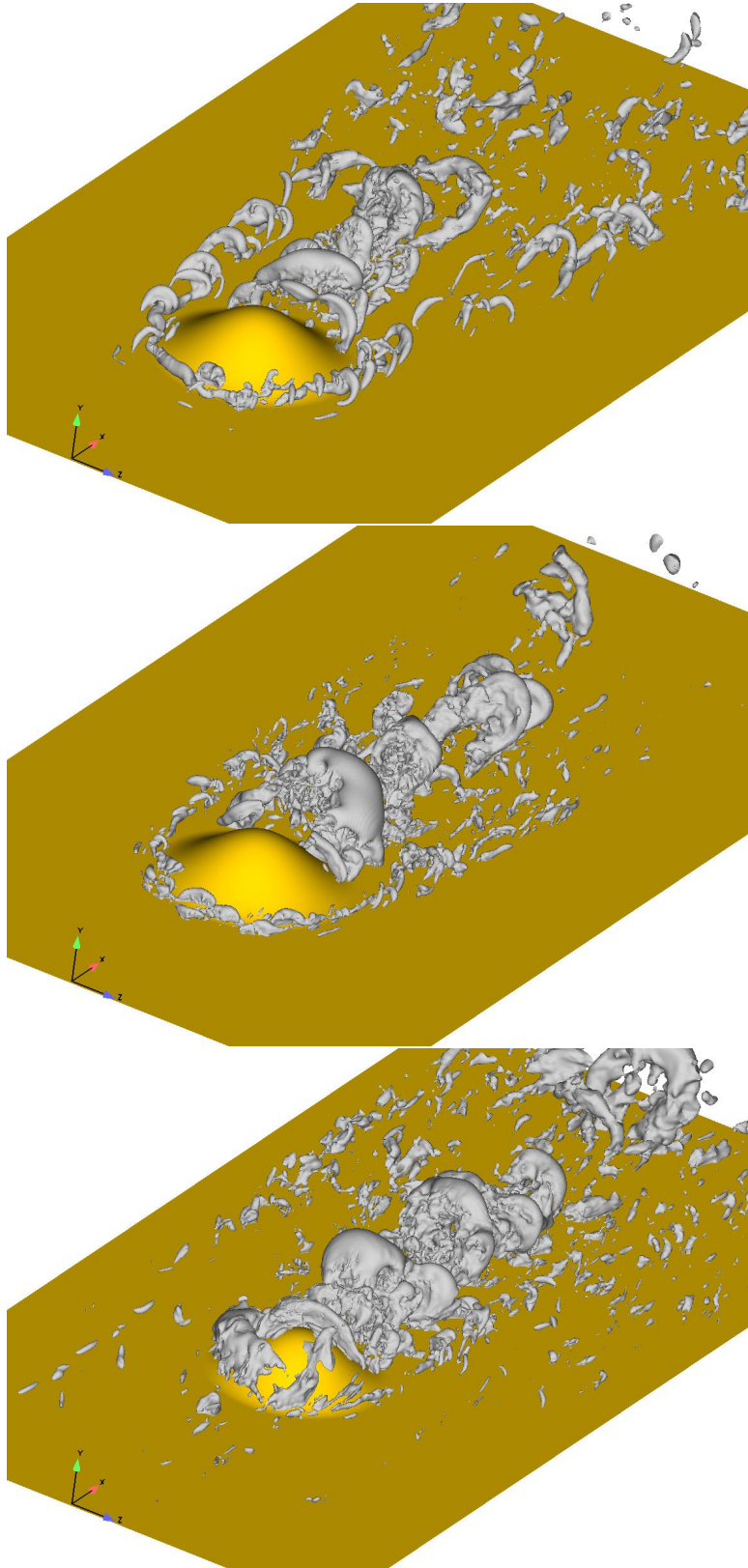


Figure 16: Iso-surface of pressure fluctuations. Top, S1- Middle, S2. Bottom, S3.

significant variations as well. All these fine details indicate that, when trying to reproduce physical experiments, special care has to be taken concerning the modelling of the inflow conditions in order to avoid observable differences in the region of interest.

## Acknowledgments

The authors are grateful to the steering committee of the supercomputing facilities in Stuttgart for granting computing time on the NEC SX-8. MGW acknowledges the financial support of the German Research Foundation (DFG).

## References

- M. S. Acarlar and C. R. Smith. A study of hairpin vortices in a laminar boundary layer. Part 1. Hairpin vortices generated by a hemisphere protuberance. *J. Fluid Mech.*, 175:1–41, 1987.
- J. Andreopoulos and J. H. Agui. Wall-vorticity flux dynamics in a two-dimensional turbulent boundary layer. *J. Fluid Mech.*, 309:45–84, 1986.
- M. Breuer and W. Rodi. Large eddy simulation of complex turbulent flows of practical interest. In E.H. Hirschel, editor, *Flow simulation with high performance computers II*, volume 52 of *Notes on Numerical Fluid Mechanics*, pages 258–274. Vieweg, Braunschweig, 1996.
- G. Byun and R. L. Simpson. Structure of three-dimensional separated flow on an axisymmetric bump. *AIAA J.*, 44(5):999–1008, 2006. (Also AIAA paper no. 2005-0113).
- G. Byun, R. L. Simpson, and C. H. Long. Study of vortical separation from three-dimensional symmetric bumps. *AIAA J.*, 42(4):754–765, 2004.
- J. Fröhlich, C. P. Mellen, W. Rodi, L. Temmerman, and M. A. Leschziner. Highly resolved large-eddy simulation of separated flow in a channel with streamwise periodic constrictions. *J. Fluid Mech.*, 526:19–66, 2005.
- M. García-Villalba, J. Fröhlich, and W. Rodi. Identification and analysis of coherent structures in the near field of a turbulent unconfined annular swirling jet using large eddy simulation. *Phys. Fluids*, 18:055103, 2006.
- M. García-Villalba, N. Li, W. Rodi, and M. A. Leschziner. Large eddy simulation of separated flow over a three-dimensional axisymmetric hill. *J. Fluid Mech.*, 627:55–96, 2009.
- M. Germano, U. Piomelli, P. Moin, and W.H. Cabot. A dynamic subgrid-scale eddy viscosity model. *Phys. Fluids*, 3:1760–1765, 1991.
- C. Hinterberger. *Dreidimensionale und tiefengemittelte Large-Eddy-Simulation von Flachwasserströmungen*. PhD thesis, University of Karlsruhe, 2004.
- J. C. R. Hunt and W. H. Snyder. Experiments on stably and neutrally stratified flow over a model three-dimensional hill. *J. Fluid Mech.*, 96:671–704, 1980.
- J. C. R. Hunt, C. J. Abell, J. A. Peterka, and H. Woo. Kinematical studies of the flow around free or surface-mounted obstacles; applying topology to flow visualization. *J. Fluid Mech.*, 86:179–200, 1978.
- S. Krajnović. Large eddy simulation of the flow around a three-dimensional axisymmetric hill. *Flow Turbulence and Combustion*, 81(1-2):189–204, 2008.

- R. Ma and R. L. Simpson. Characterization of turbulent flow downstream of a three-dimensional axisymmetric bump. In *Proc. 4th Int. Symposium on Turbulence and Shear Flow Phenomena. Williamsburg, Virginia, USA*, pages 1171–1176, 2005.
- R. Martinuzzi and C. Tropea. The flow around surface-mounted, prismatic obstacles placed in a fully-developed channel flow. *J. Fluids Eng.*, 115:85–92, 1993.
- G. Palau-Salvador, T. Stoesser, J. Fröhlich, M. Kappler, and W. Rodi. Large eddy simulations and experiments of flow around finite-height cylinders. *Flow Turbulence and Combustion*, 84(2):239–275, 2010.
- R. L. Panton. *Incompressible flow*. John Wiley & Sons, 1984.
- N. Patel and S. Menon. Structure of flow separation and reattachment behind an axisymmetric hill. *J. Turbulence*, 8(36):1–24, 2007.
- T. Persson, M. Liefvendahl, R. E. Benson, and C. Fureby. Numerical investigation of the flow over an axisymmetric hill using LES, DES and RANS. *J. Turbulence*, 7(4):1–17, 2006.
- C.D. Pierce. *Progress-variable approach for large-eddy simulation of turbulent combustion*. PhD thesis, Stanford University, 2001.
- C. M. Rhie and W. L. Chow. Numerical study of the turbulent flow past an airfoil with trailing edge separation. *AIAA J.*, 21(11):1061–1068, 1983.
- R. L. Simpson, C. H. Long, and G. Byun. Study of vortical separation from an axisymmetric hill. *Int. J. Heat Fluid Flow*, 23(5):582–591, 2002.
- P. R. Spalart. Direct simulation of a turbulent boundary layer up to  $Re_\theta = 1410$ . *J. Fluid Mech.*, 187: 61–98, 1988.
- H.L. Stone. Iterative solution of implicit approximations of multidimensional partial differential equations for finite difference methods. *SIAM J. Numer. Anal.*, 5:530–558, 1968.
- F. Tessicini, N. Li, and M. A. Leschziner. Large-eddy simulation of three-dimensional flow around a hill-shaped obstruction with a zonal near-wall approximation. *Int. J. Heat Fluid Flow*, 28(5): 894–908, 2007.
- C. Wang, Y. J. Jang, and M. A. Leschziner. Modelling two- and three-dimensional separation from curved surfaces with anisotropy-resolving turbulence closures. *Int. J. Heat Fluid Flow*, 25(3):499–512, 2004.
- J. G. Wissink. DNS of separating, low Reynolds number flow in a turbine cascade with incoming wakes. *Int. J. Heat Fluid Flow*, 24:626–635, 2003.
- J. G. Wissink, H.P. Hodson, and W. Rodi. The influence of disturbances carried by periodically incoming wakes on the separating flow around a turbine blade. *Int. J. Heat Fluid Flow*, 27:721–729, 2006.